



Automatic strain sensor design via active learning and data augmentation for soft machines

Haitao Yang^{1,7}, Jiali Li^{1,7}, Kai Zhuo Lim¹, Chuanji Pan¹, Tien Van Truong², Qian Wang¹, Kerui Li¹, Shuo Li¹, Xiao Xiao³, Meng Ding¹, Tianle Chen⁴, Xiaoli Liu¹, Qian Xie⁵, Pablo Valdivia y. Alvarado⁶, Xiaonan Wang⁶✉ and Po-Yen Chen⁴✉

Emerging soft machines require high-performance strain sensors to achieve closed-loop feedback control. Machine learning is a versatile tool to uncover complex correlations between fabrication recipes and sensor performance at the device level. Here a three-stage machine learning framework was realized for a high-accuracy prediction model capable of automating the design of strain sensors. First, a support-vector machine classifier was trained by using 351 compositions of various nanomaterials. Second, through 12 active learning loops, 125 strain sensors were stagewise fabricated to enrich the multidimensional dataset. Third, to address the challenge of data scarcity, data augmentation was implemented to synthesize >10,000 virtual data points, followed by genetic algorithm-based selection to optimize the model's prediction accuracy. Several data-driven design rules for piezoresistive nanocomposites were generalized and validated by in situ microscopic studies. As final demonstrations, model-suggested strain sensors can be integrated into/onto various soft machines to endow them with real-time strain-sensing capabilities.

Emerging soft machines exhibit outstanding compliance^{1,2}, excellent adaptability^{3,4} and evenly distributed force^{5,6}, which provide safer human-machine interfaces than conventional stiff machines^{7,8}. To enable soft machines to respond intelligently to their environment, high-precision sensing technologies are the essential components to transduce a variety of mechanical/environmental stimuli into electrical signals^{9–11}. Compliant strain sensors offer real-time sensing capabilities and can achieve closed-loop feedback control in various domains of sensor-integrated soft machines, ranging from ultra-gentle manipulation^{12,13} to artificial muscles^{14,15} and soft prostheses^{16,17}. Due to the soft and stretchy robotic body that enables programmable actuating behaviours across a wide strain range, several challenges exist in the design of strain sensors for diverse soft machines. First, many of the reported strain sensors focused on monitoring the strain changes from 30% to 200%^{18–24}, whereas few strategies were developed to fabricate the strain-sensing devices with high sensitivity at extremely low (<5%)²⁵ and ultra-high strains (>300%)^{26,27}. Second, to monitor the coordinated motions of a soft machine, multiple compliant strain sensors with different working windows are often demanded to be integrated at separate robotic units with distinct actuating behaviours^{28,29}. Different design principles often need to be adopted to fabricate the strain sensors with user-designated characteristics^{18,19}, and multiple trial-and-error experiments should be conducted to validate the sensing performance^{20,21}. To facilitate the custom production of sensor-integrated soft machines, an automatic design approach is highly desired, where feasible fabrication recipes can be suggested to obtain adequate strain sensors for a variety of sensing tasks.

Machine learning is a versatile tool that builds up a model to make predictions or recommendations^{30,31}, which has been

particularly appropriate for the data-rich systems to uncover underlying trends and investigate complex correlations³². The exploitation of machine intelligence to research in the materials science has gained many interests in the subjects of organic/inorganic catalyst design^{33–35}, drug discovery^{36,37} and quantum dot synthesis^{38,39}, where a large number of data points can be supplied either computationally or analytically⁴⁰. By contrast, at the device level, the data acquisition rate is largely limited by the scarcity of high-quality data^{41,42}. Substantial obstacles to developing a prediction model with high accuracy thus exist in the subject of automatic strain sensor design. First, there are no standardized protocols for the fabrication/characterization of soft strain sensors^{19,43}, and different research laboratories come up with their own fabrication schemes^{18,19}. Thus, the sensor data collected from the literature are not very consistent and may contain bias. Second, most of recent reports focused on the fabrication of strain sensors enabling real-time monitoring of in-plane strains between 30% to 200%^{18–24}. Such unbalanced data is likely to produce a machine learning model with restricted prediction capabilities within specific strain ranges⁴⁴, which would not benefit the strain sensor design for many soft machines at extreme strain cases (for example, <5% or >300%). Third, the fabrication of soft strain sensors is normally tedious and time-consuming⁴³, and thus the data acquisition rate is low, making the machine learning model fall short of data points and present insufficient prediction accuracy⁴⁵. As a result, it is of high value to address these challenges through a hybrid approach (experimentally and computationally) for construction of a machine learning model at device level, which can realize the concept of automatic strain sensor design for diverse soft machines.

Herein, to develop a prediction model capable of automating the design of strain sensors, a three-stage machine learning framework

¹Department of Chemical and Biomolecular Engineering, National University of Singapore, Singapore, Singapore. ²Engineering Product Development, Singapore University of Technology and Design, Singapore, Singapore. ³Department of Electrical and Electronic Engineering, Southern University of Science and Technology, Shenzhen, China. ⁴Department of Chemical and Biomolecular Engineering, University of Maryland, College Park, MD, USA. ⁵School of Metallurgical Engineering, Anhui University of Technology, Ma'anshan, China. ⁶Department of Chemical Engineering, Tsinghua University, Beijing, China. ⁷These authors contributed equally: Haitao Yang, Jiali Li. ✉e-mail: wangxiaonan@tsinghua.edu.cn; checp@umd.edu

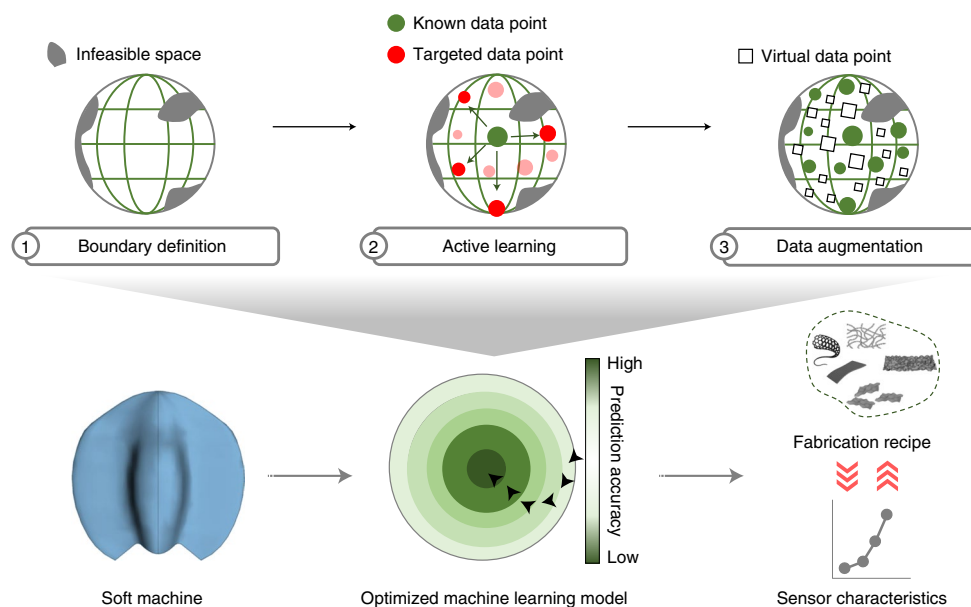


Fig. 1 | Three-stage framework for construction of a machine learning-enabled prediction model capable of automatic strain sensor design for soft machines. Three steps were conducted sequentially to develop an ultimate prediction model with the assistance of machine intelligence, including boundary definition, active learning, and data augmentation with genetic algorithm selection.

was realized in Fig. 1, including boundary definition, active learning and data augmentation. The machine learning-enabled prediction model was able to execute two-way tasks of automatic strain sensor design, including (1) high-accuracy sensor performance prediction based on a proposed fabrication recipe and (2) recommendation of feasible fabrication recipes to obtain adequate strain sensors for monitoring a specific soft machine.

Results

Influential fabrication parameters for tuning strain sensor characteristics. Two characteristics of a strain sensor are generally evaluated, including strain sensitivity and working window. The sensitivity of a strain sensor is characterized by gauge factor (GF), as defined in equation (1):

$$GF = \frac{(R - R_0)/R_0}{\varepsilon}, \quad (1)$$

where ε denotes the applied uniaxial strain, and R_0 and R represent the initial resistance and the resistance under strain, respectively. On the other hand, the working window of a strain sensor is determined by the strain range where the resistance of the sensing layer increased with the applied strain. When the strain sensor reaches its maximal resistance, the maximal working strain is abbreviated as ε_{\max} .

In this Article, three building blocks—single-walled carbon nanotubes (SWNTs), $\text{Ti}_3\text{C}_2\text{T}_x$ MXene nanosheets and polyvinyl alcohol (PVA)—were selected for the fabrication of strain-sensing layers (Extended Data Fig. 1a). Detailed characterizations of SWNTs and MXene nanosheets are provided in Supplementary Fig. 1. The mixture of MXene nanosheets, SWNTs and PVA was next prepared (as shown in Supplementary Fig. 2a) and underwent vacuum-assisted filtration to deposit a composite layer of MXene/SWNT/PVA (hereafter abbreviated as the ps-MXene layer) on a polyvinylidene fluoride (PVDF) membrane. Supplementary Fig. 2b–f presents a detailed materials characterization of a ps-MXene layer.

The as-filtered ps-MXene layer was next immersed in an ethanol bath to detach it from the PVDF membrane. The freestanding

and planar ps-MXene layer was then transferred onto an elastomeric substrate (that is, VHB tape) for the fabrication of a G_0 sensor, where G_0 indicates that the sensing layer did not experience any pre-deformations (see Supplementary Fig. 3 for details)⁴⁶. As shown in Extended Data Fig. 1b,c, with different compositions and thicknesses in the strain-sensing layers, the resistance–strain profiles of the resulting G_0 sensors were affected in a non-linear manner.

Another approach to tuning the sensor characteristics is through engineering the surface morphology of a strain-sensing layer. As described in the Methods, through controlled uniaxial or biaxial thermal shrinkage, the planar ps-MXene layer was deformed into periodic wrinkles (named G_1 -1D) or isotropic crumples (G_1 -2D) (see the scanning electron microscope (SEM) images in Supplementary Figs. 4 and 5). After transferring micro-textured ps-MXene layers onto VHB tapes, G_1 -1D and G_1 -2D sensors were obtained (detailed fabrication in Supplementary Fig. 6). As shown in Extended Data Fig. 1d, at the same composition and thickness of ps-MXene layers (100/0/0, 800 nm), the ε_{\max} values of the G_0 , G_1 -1D and G_1 -2D sensors were characterized as 10%, 37% and 120%, respectively. With different surface morphologies, the G_0 , G_1 -1D and G_1 -2D sensors exhibited different fracture mechanisms, as discussed in Supplementary Note 1 and Supplementary Fig. 7. A rough estimation of the number of G_n sensors required for an extensive reference dataset was described in Supplementary Note 2.

Boundary definition in sensor design space through a support-vector machine. At the first stage of boundary definition (Fig. 2a), a series of MXene/SWNT/PVA mixtures with different ratios were deposited on PVDF membranes to obtain various ps-MXene layers (at fixed thicknesses of 800 nm). Three different detachment scenarios from PVDF membranes in ethanol were observed: (1) complete detachment (feasible cases); (2) detachment with visible fractures (fragile cases); and (3) sticking on PVDF membranes (failed cases). Only the feasible cases were valid to proceed with further strain sensor fabrication; 351 mixtures were examined and the grades of detachment feasibility were summarized in Fig. 2b and Supplementary Table 1.

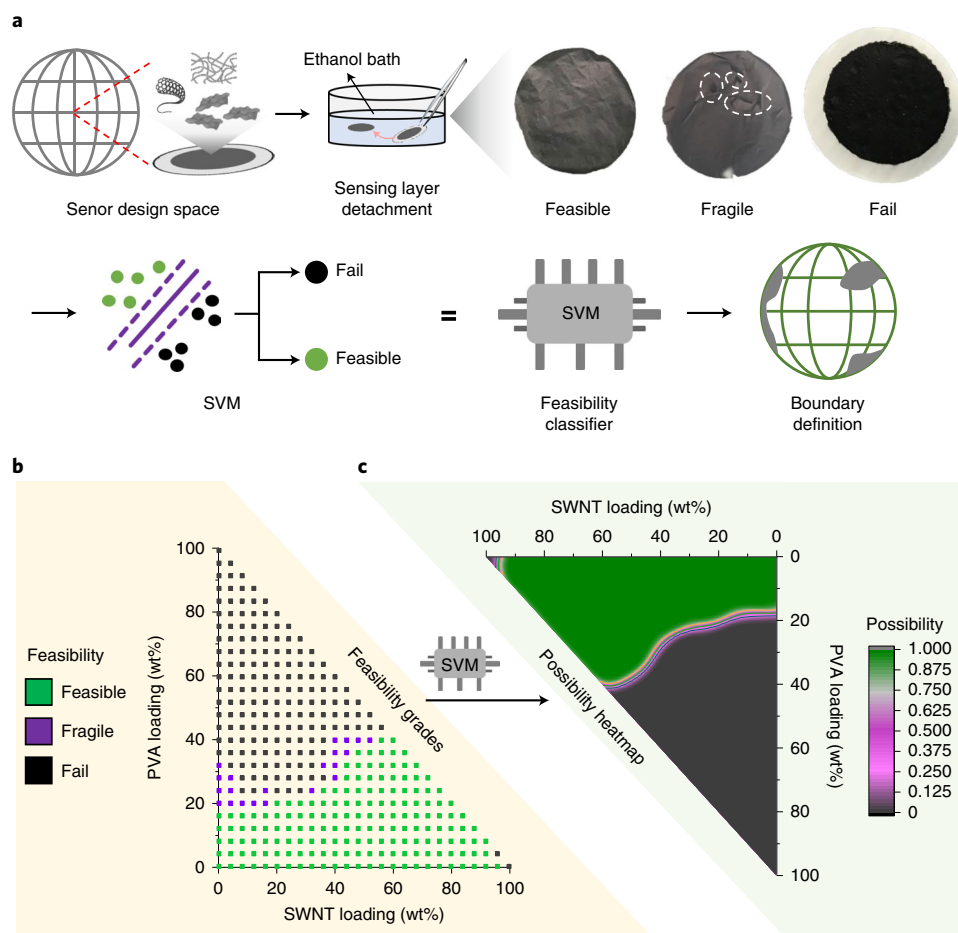


Fig. 2 | Boundary definition in sensor design space through an SVM. **a**, Schematic illustration of the training process of an SVM classifier to define multi-degree of freedom boundaries of sensor design space. **b**, Feasibility grades of detachment situations of 351 ps-MXene layers (at different SWNT and PVA loadings) from PVDF membranes. Step sizes for the changes of both SWNT and PVA loadings were set to be 4.0 wt%. **c**, Possibility heatmap representing the chances of successfully detaching ps-MXene layers (at different SWNT and PVA loadings) from PVDF membranes.

These feasibility grades at various MXene/SWNT/PVA ratios were utilized as the input data points to train a support-vector machine (SVM) classifier (see Supplementary Note 3 for a detailed description)⁴⁷. The trained SVM classifier was able to transform discrete feasibility grades into a possibility heatmap that represented the chances of successfully detaching ps-MXene layers from PVDF membranes (Fig. 2c). The trained SVM classifier served as a critical unit in the active learning loops at the second stage, which performed as a screening layer and drove the machine learning model to only recommend the fabrication recipes with high detachment possibilities. The necessity of the SVM classifier is described in Supplementary Note 4.

Progressive exploration of sensor design space through active learning. At the second stage of space exploration, we executed multiple loops of active learning to collect representative data points within the multi-degree of freedom design space and construct a machine learning-enabled model (called a navigation model; Fig. 3a). Several terms used in the active learning loops are explained in Supplementary Note 5. First, 11 fabrication recipes were randomly selected to obtain five G_0 , three G_1 -1D and three G_1 -2D sensors, and their resistance-strain profiles were then characterized. For each profile, four representative sensor characteristics were recognized, including initial strain (ϵ_0), strain at a GF of 10 (ϵ_{10}), strain at a GF of 100 (ϵ_{100}) and ultimate strain (ϵ_{\max}).

These four strain labels (ϵ_0 , ϵ_{10} , ϵ_{100} and ϵ_{\max}) were then bundled with four recipe labels (SWNT loading, PVA loading, sensing layer thickness and morphology), which served as one input data point; a total of 11 data points were collected.

For the construction of a navigation model, 11 data points were first input into the nonlinear algorithms of an artificial neural network (ANN) and a decision tree to train six decision programs through tenfold cross-validation. These decision programs were designed to calculate an acquisition function (called the A-Score, defined in equation (2)) to evaluate the unfamiliarity level of a targeted region in the sensor design space:

$$\text{A-Score} = L_2 \times \hat{\sigma}, \quad (2)$$

where L_2 denotes the shortest mathematical distance between current recipe labels (within the dataset of navigation model) and targeted recipe labels (not yet included in the current dataset), and $\hat{\sigma}$ denotes the variance of predicted strain labels from six decision programs (see Supplementary Note 6 for a detailed calculation). After the calculation of A-Scores for 11 data points, the preliminary navigation model suggested the targeted data points with the highest A-Scores for the first loop of active learning, to explore the most unfamiliar regions with high uncertainty and far from current model. We also tested other acquisition functions (for example, variance, random selection and distance), but the machine

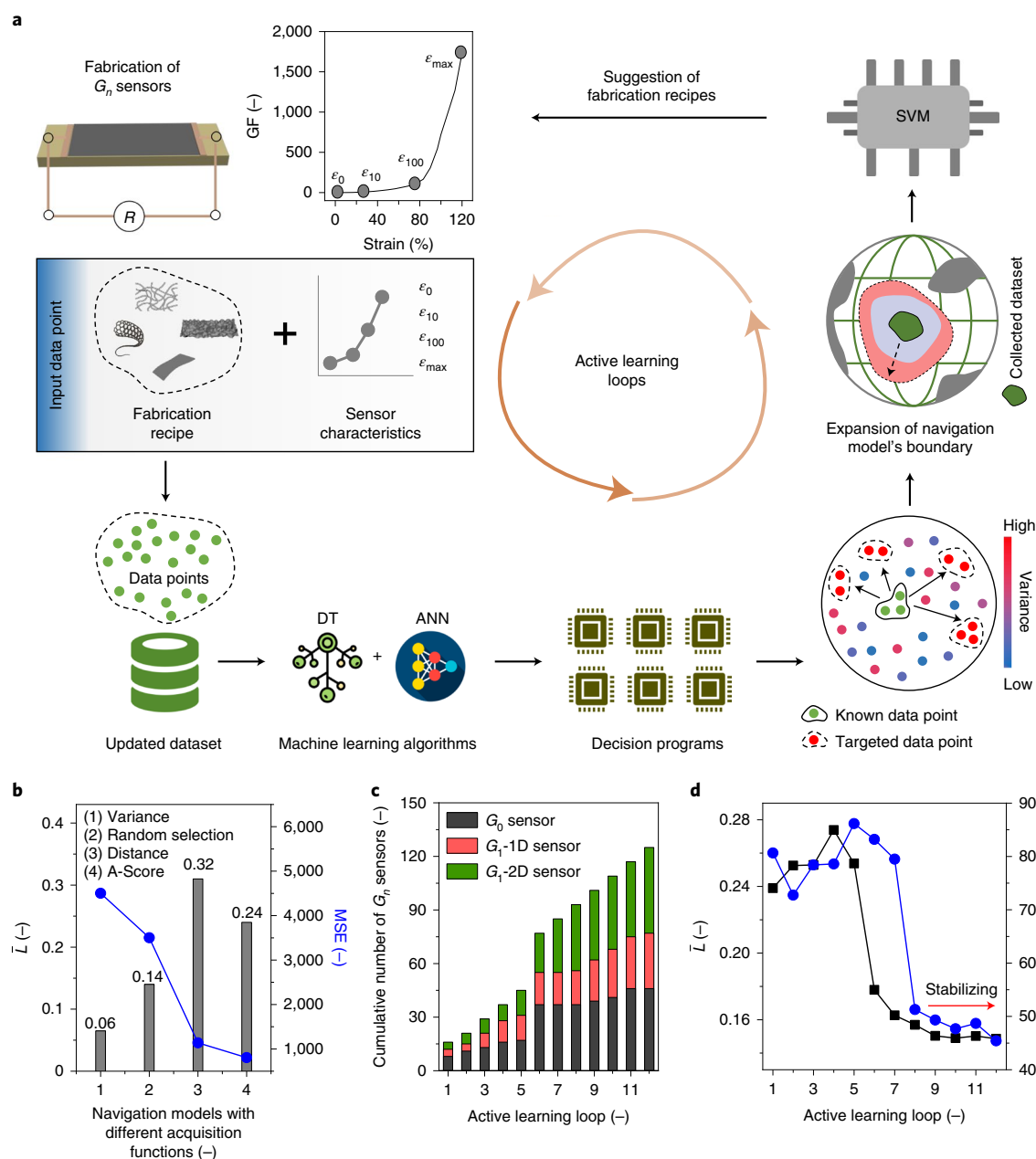


Fig. 3 | Progressive exploration of sensor design space through active learning. **a**, Schematic illustration of construction process of a navigation model through active learning loops. Each data point contains eight labels, including four recipe labels (SWNT loading, PVA loading, sensing layer thickness and morphology) and four strain labels (ϵ_0 , ϵ_{10} , ϵ_{100} and ϵ_{\max}). **b**, \bar{L} and MSE values of trained navigation models by using different acquisition functions, including variance, random selection, distance and A-Score. The navigation model on basis of A-Score-based acquisition function showed the largest \bar{L} and the lowest MSE after one active learning loop. **c**, Cumulative number of fabricated G_n sensors for each loop of active learning. **d**, \bar{L} and MSE values of evolving navigation model at different stages of active learning. (–) indicates that the parameter is dimensionless.

learning model using A-Score demonstrated higher learning efficiency in terms of prediction accuracy (Fig. 3b and further discussion in Supplementary Note 7).

The resistance–strain profiles of suggested G_n sensors (including three G_0 sensors, one G_1 -1D and one G_1 -2D sensor) were recorded, and four strain labels (ϵ_0 , ϵ_{10} , ϵ_{100} and ϵ_{\max}) for each sensor were recognized and then bundled with corresponding recipe labels as a new data point. After five data points were added into the dataset, the boundaries of navigation model were redefined, and the A-Scores of targeted data points were recalculated. Similarly, the navigation model suggested the targeted data points with the highest A-Scores

for the next learning loop. By repeating the active learning loops, the boundaries of navigation model expanded in a progressive manner, and more data points were included sequentially. In this work, 12 loops of active learning were executed, and a total of 125 G_n sensors (including 46 G_0 , 31 G_1 -1D and 48 G_1 -2D sensors) were fabricated (Supplementary Table 2 summarizes their recipe and strain labels). Figure 3c presents the cumulative number of model-suggested G_n sensors during the active learning loops. Further discussion regarding the selection of different training data (entire strain–resistance curves versus strain labels) is provided in Supplementary Note 8. As shown in Supplementary Note 9, Supplementary Figs. 8 and 9, the

navigation model (using ANN/decision tree committees) predicted the complex strain responses of G_n sensors better than other linear models (using linear regression algorithms).

Evolution of navigation model during active learning. The evolution of navigation model during active learning was monitored from two aspects, including (1) the degree of space exploration and (2) the prediction accuracy of sensor performance. To represent the degree of space exploration, we utilized the average mathematical distance between collected recipe labels (abbreviated as \bar{L} ; a detailed calculation is provided in the Methods). A higher \bar{L} indicates a wider distribution of data points in the sensor design space, whereas a lower \bar{L} corresponds to close clusters formed among existing data points. The difference between L_2 and \bar{L} is explained in Supplementary Note 10.

Aside from \bar{L} , the prediction accuracy of six decision programs was evaluated by using an additional 30 test data points (see Supplementary Table 3). The recipe labels of test data were input into the decision programs, and the strain labels (ϵ_{10} , ϵ_{100} and ϵ_{\max}) were predicted accordingly. The model-predicted strain labels were then compared with the actual strain values of the test data, and the deviations of strain values were quantified by using a mean squared error (MSE) (see the Methods for a detailed calculation). A smaller MSE value indicates higher prediction accuracy of decision programs and vice versa. The extra 30 test data points were only used for MSE calculation and never input for model training.

During active learning, the machine learning-enabled navigation model evolved by incorporating more representative data points into its dataset, leading to the continuous \bar{L} and MSE changes (as present in Fig. 3d). As shown in Supplementary Fig. 10, the preliminary navigation model with only 11 data points exhibited a small \bar{L} of 0.07 and a very large MSE of $\sim 2 \times 10^4$. From the second to fourth loop, \bar{L} increased to 0.27 with fluctuating MSEs at ~ 800 as the boundaries of navigation model continued to expand. From the ninth loop onwards, both \bar{L} and MSE stabilized at 0.15 and 454, respectively. After 12 loops of active learning, the navigation model was able to predict the characteristics of the G_n sensors to some extent (Supplementary Fig. 11). To further reduce the deviations between model-predicted and actual sensor performance, we expected that $>1,000$ G_n sensors were required to be fabricated, which was impractical to achieve. In silico approaches (for example, data augmentation) were therefore adopted to optimize the machine learning-enabled prediction model.

Model optimization through data augmentation and GA selection. Figure 4a illustrates the optimization process to develop an ultimate prediction model through sequential steps of data augmentation and genetic algorithm (GA) selection. Two data augmentation methods—the Synthetic Minority Oversampling Technique for Regression (SMOTE-REG) and User Input Principle (UIP)—were introduced to synthesize virtual data points (see Supplementary Note 11 for a detailed description). Both the SMOTE-REG and UIP methods increased the total amount of data points (real and virtual) by two orders of magnitude; that is, from 125 to $\sim 10,000$.

These augmented data points were then input into a decision tree and ANN to produce two large pools of decision programs (300 per pool) followed by GA selection that mimics biological evolution⁴⁸. A detailed description of the GA selection method is provided in Supplementary Note 11. According to Fig. 4a, GA selection picked up a set of decision programs from each pool to construct multiple candidate models followed by accuracy ranking (using validation data). Thereafter, an extra test set consisting of 30 additional data points (in Supplementary Table 3) was used to evaluate the model prediction accuracy, and the mean relative error (MRE) between

predicted strain labels and actual strain values was calculated in equation (3):

$$\text{MRE} = \sum_{i=1}^N \frac{|\epsilon_{10}^i - E_{10}^i| + |\epsilon_{100}^i - E_{100}^i| + |\epsilon_{\max}^i - E_{\max}^i|}{3E_{\max}^i}, \quad (3)$$

where N is the cumulative number of test data ($N=30$); ϵ_{10}^i , ϵ_{100}^i and ϵ_{\max}^i are the model-predicted strain labels on basis of the recipe labels of a test data point i ; and E_{10}^i , E_{100}^i and E_{\max}^i are the actual strain values from a test data point i . The selection of MRE over MSE as the loss function is discussed in Supplementary Note 12. More discussion about the prediction sequence of strain labels is described in Supplementary Note 13.

As shown in Fig. 4b, the candidate model with the best prediction performance was constructed through the UIP method followed by GA selection (abbreviated as prediction model (UIP + GA)), which demonstrated the lowest MRE of 24% (see the model-predicted strain labels in Supplementary Table 4) and served as an ultimate prediction model for automatic sensor design afterwards. Figure 4c–e further demonstrates the predicted sensor labels of the G_0 , G_1 -1D and G_1 -2D sensors generated from prediction model (UIP + GA) and various candidate models, where the deviations between the actual GF-strain curves and the predicted results continued to reduce after the implementation of data augmentation and GA selection (further discussion in Supplementary Note 11).

Statistical analysis of data points collected from active learning.

Aside from the development of an ultimate prediction model for automatic sensor design, we conducted statistical analyses on 125 data points to find out whether there are any usable design principles for future reference. First, the navigation model suggested >110 fabrication recipes to obtain G_n sensors with ϵ_{\max} ranging from 3.3% to 350% (Fig. 5a). The results indicate that the machine learning model did explore a wide strain range. We categorized the data points into G_0 , G_1 -1D, G_1 -2D sensors in Fig. 5b, where several design principles were generalized in Supplementary Note 14.

Next, Spearman's rank correlation coefficient (abbreviated as Spearman's ρ ; see Supplementary Note 15 for a detailed description) was introduced to statistically assess the nonlinear correlations between fabrication recipes and sensor characteristics⁴⁹. For G_1 -2D sensors (Fig. 5c), SWNT loading was more influential on ϵ_{\max} than PVA loading and sensing layer thickness. Furthermore, according to the Spearman's ρ results for G_1 -1D sensors (Fig. 5d), comparably strong were observed from SWNT loading and sensing layer thickness on ϵ_{\max} , whereas for G_0 sensors (Fig. 5e), strong correlation existed between sensing layer thickness and ϵ_{\max} .

In addition to Spearman's ρ analyses, we further investigated the complex correlations between fabrication recipes and sensor characteristics by using Shapley Additive Explanations (abbreviated as SHAP; see Supplementary Note 16 for a detailed description)^{50–52}. To identify which fabrication parameters are the most impactful to a specific strain label (that is, ϵ_{\max}), in Fig. 5f–h we calculated the SHAP values of SWNT loading, PVA loading and layer thickness on ϵ_{\max} for each G_n sensor type. According to the analyses in Supplementary Note 17 and Supplementary Table 5, both Spearman's ρ and SHAP analyses led to similar conclusions: (1) SWNT loading was the most influential parameter for the ϵ_{\max} of G_1 -2D sensors; (2) SWNT loading and sensing layer thickness showed comparably large influences on the ϵ_{\max} of G_1 -1D sensors; and (3) sensing layer thickness was the most influential parameter on the ϵ_{\max} of G_0 sensors.

In situ electron microscopic studies to validate data-driven design rules. The data-driven design rules were next validated by performing in situ electron microscopic studies to investigate the piezoresistive

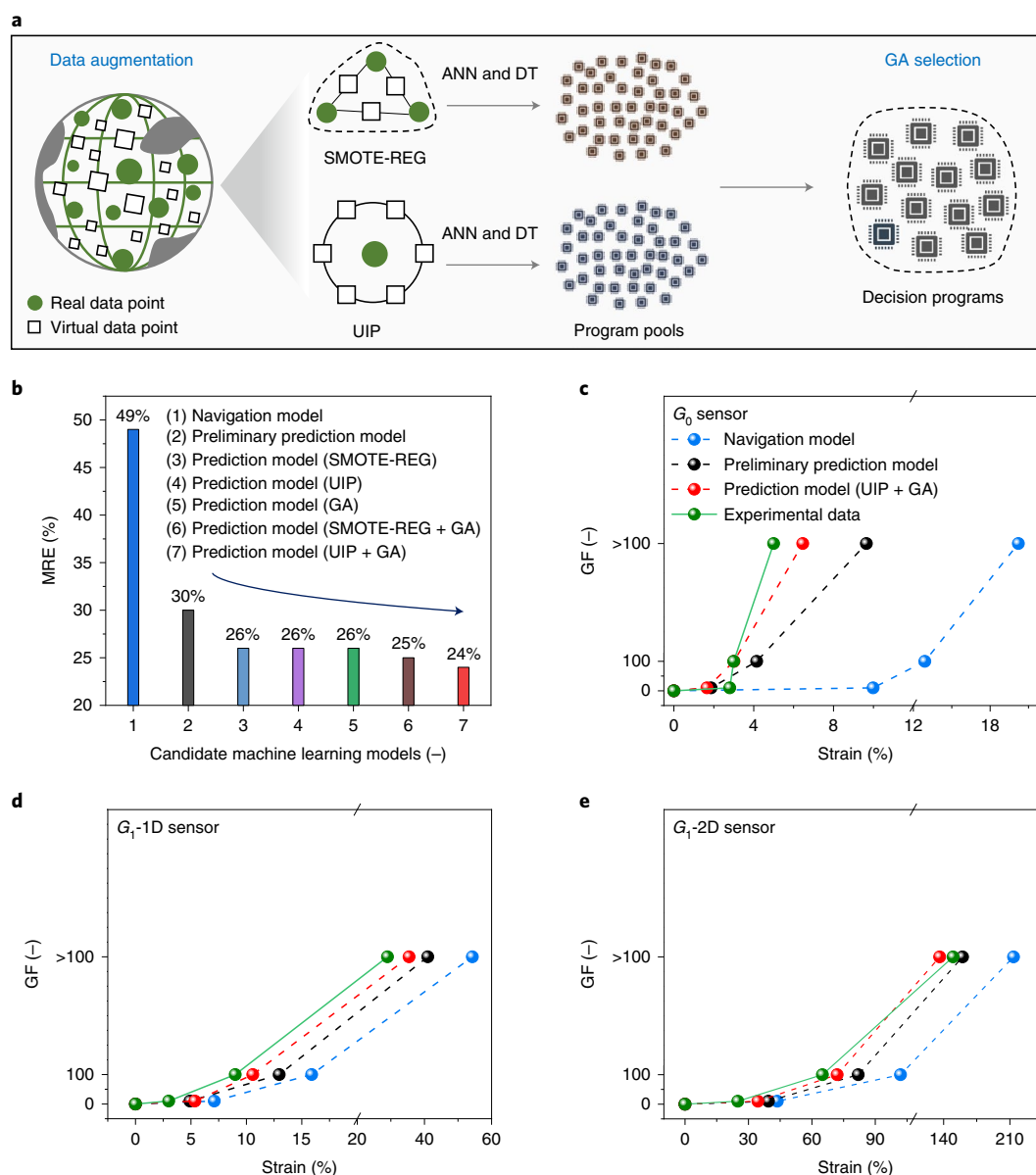


Fig. 4 | Model optimization through data augmentation and GA-based selection. **a**, Schematic illustration of construction and optimization processes of an ultimate prediction model through data augmentation and GA-based selection. **b**, Comparison of MRE values of various candidate models. Navigation model, the machine learning model after active learning loops on basis of MSE loss function; preliminary prediction model, machine learning model prior to data augmentation and GA selection on basis of MRE loss function; prediction model (SMOTE-REG), machine learning model after data augmentation with the method of SMOTE-REG (without GA selection); prediction model (UIP), machine learning model after data augmentation with the method of UIP (without GA selection); prediction model (GA), machine learning model after GA selection only (without data augmentation); prediction model (SMOTE-REG + GA), machine learning model after SMOTE-REG method and GA selection; prediction model (UIP + GA), machine learning model after the UIP method and GA selection. **c**, Model-predicted strain labels and actual sensor characteristics of a G_0 sensor (with a MXene/SWNT/PVA ratio of 69/13/18 and a sensing layer thickness of 954 nm). **d**, Model-predicted strain labels and actual sensor characteristics of a G_1 -1D sensor (with a MXene/SWNT/PVA ratio of 12/84/4 and a sensing layer thickness of 465 nm). **e**, Model-predicted strain labels and actual sensor characteristics of a G_1 -2D sensor (with a MXene/SWNT/PVA ratio of 100/0/0 and a sensing layer thickness of 200 nm).

mechanisms from the mechanics and physics perspectives. Extended Data Fig. 2a recorded the cracks propagation behaviours of planar ps-MXene layers with varying layer thicknesses from 400 to 1,600 nm. As shown in Extended Data Fig. 2b, the increase of crack-to-width ratio (defined as the ratio of the length of the longest crack to the active layer width) of the 1,600-nm-thick active layer was much faster than the one of 400-nm-thick layer. Meanwhile, the maximal crack density (defined as the maximal cumulative length of cracks per unit area) of the active layers increased from 487 to

2,038 $\mu\text{m mm}^{-2}$ (Extended Data Fig. 2c). On the other hand, according to Supplementary Fig. 12, for planar ps-MXene layers with varying SWNT loadings from 10 wt% to 60 wt%, the crack-to-width ratios of the three active layers increased similarly with the applied strains (Extended Data Fig. 2d), and their maximal crack densities were nearly the same at 500 $\mu\text{m mm}^{-2}$ (Extended Data Fig. 2e). As further shown in Supplementary Table 6, the layer thickness provided more dominant effects than the SWNT loadings for the ε_{max} of G_0 sensors.

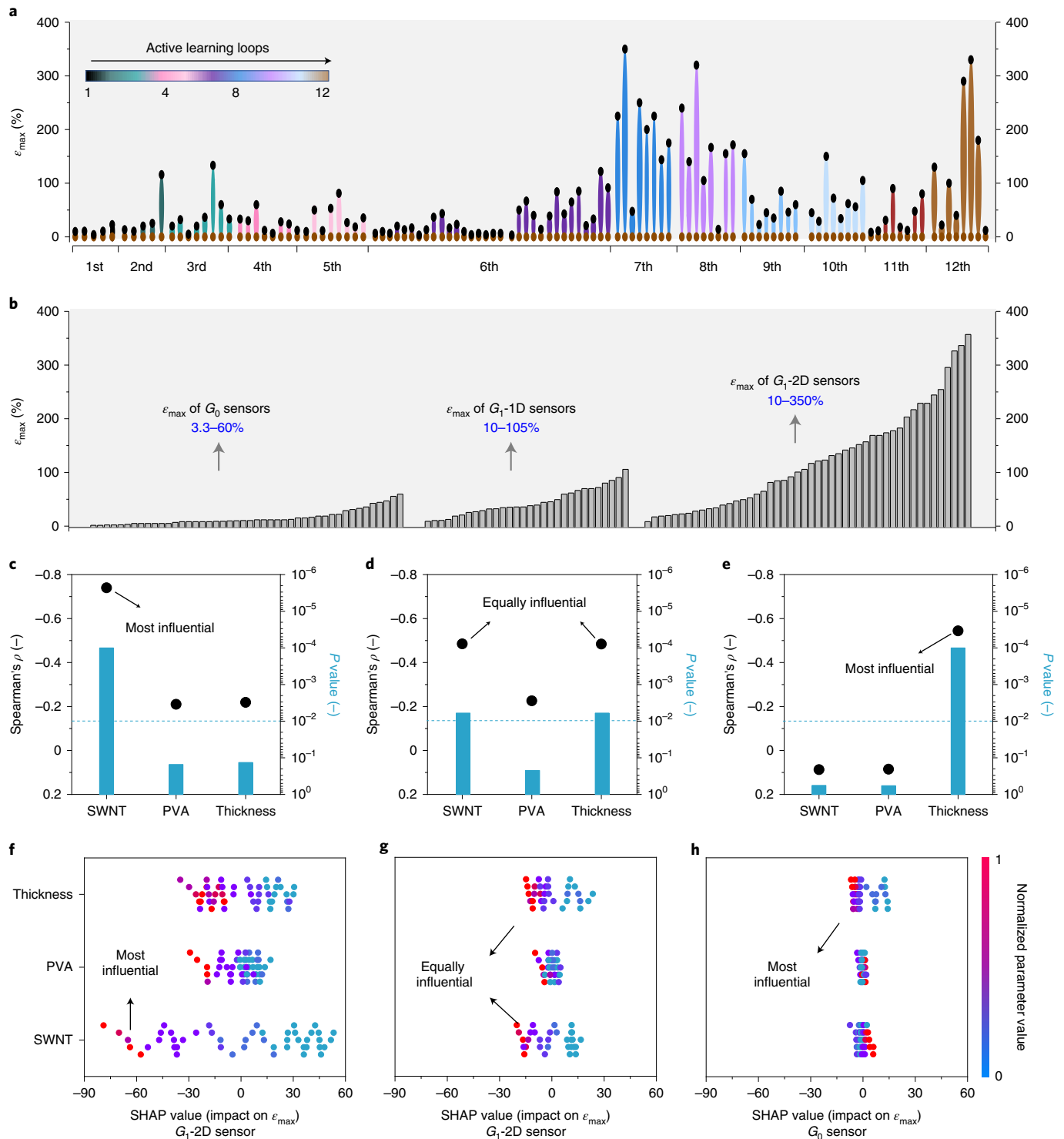


Fig. 5 | Statistical analysis of data points collected from active learning. **a**, Classification of ϵ_{\max} extracted from all G_n sensors at different stages of active learning. **b**, Classification of ϵ_{\max} extracted from 125 G_n sensors at different morphologies of strain-sensing layers. Spearman's ρ statistical analyses for G_1 -2D (**c**), G_1 -1D (**d**) and G_0 (**e**) sensors between fabrication parameters (for example, SWNT loading, PVA loading and sensing layer thickness) and ϵ_{\max} . **f**, SHAP values of SWNT loading, PVA loading and sensing layer thickness for G_1 -2D sensors. **g**, SHAP values of SWNT loading, PVA loading and sensing layer thickness for G_1 -1D sensors. **h**, SHAP values of SWNT loading, PVA loading and sensing layer thickness for G_0 sensors.

We next conducted in situ electron microscopic studies and finite element analyses (FEAs) to investigate how the layer morphology affected the crack propagation behaviours of G_n sensors (Extended Data Fig. 2f–h). For the G_0 layer, large and localized strain was observed in the central region under 15% uniaxial strain, leading

to long and continuous cracks. For the G_1 -1D layer, the localized strain was much smaller than the G_0 case under 20% uniaxial strain due to the deformation of pre-existed micro-wrinkles, leading to short and zigzagged cracks. For the G_1 -2D layer, the crack propagation behaviours were further delayed under in-plane strains, and

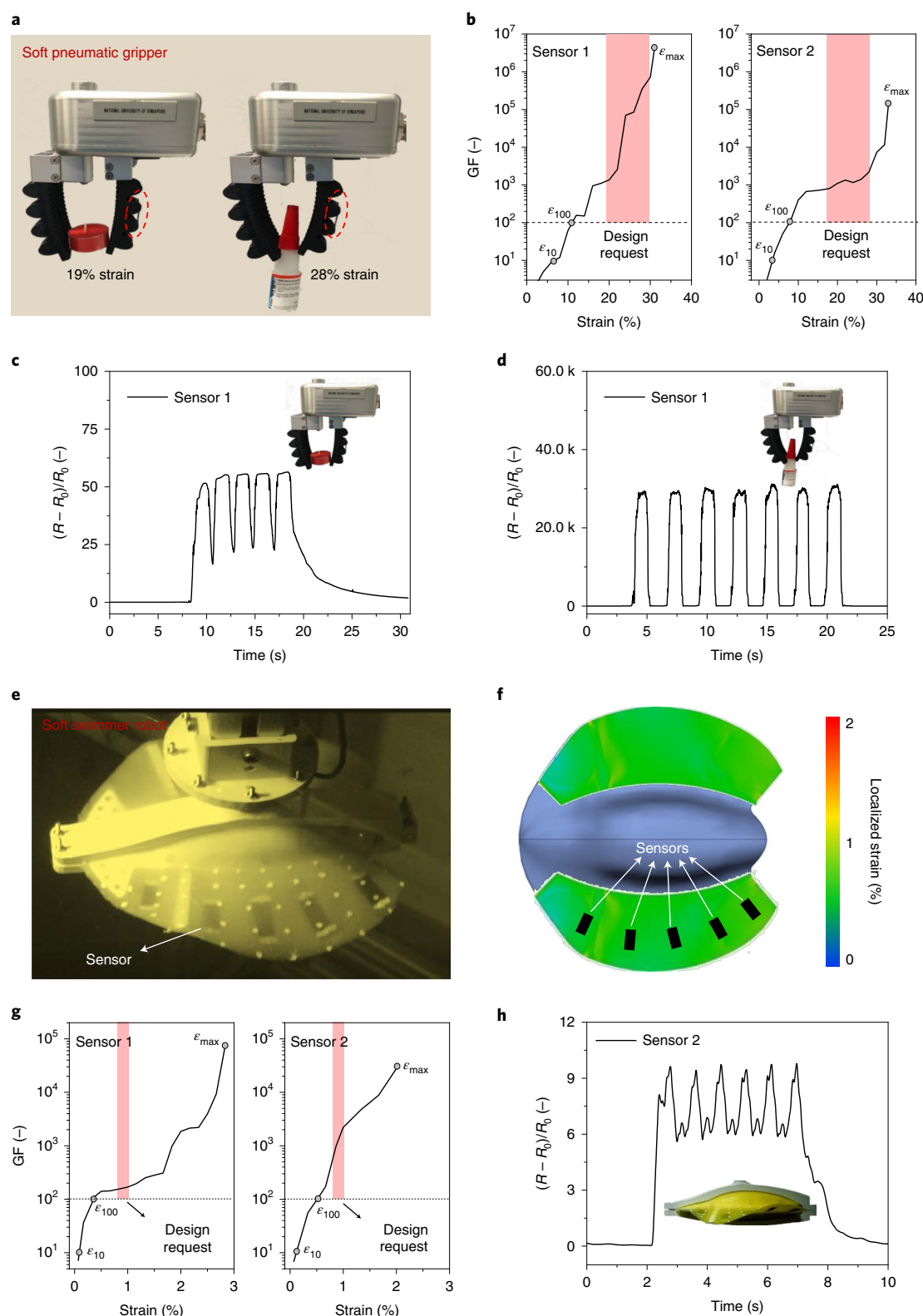


Fig. 6 | Automatic sensor design for soft machines. **a**, Soft pneumatic gripper grasped a candle and a glue with respective 19% and 28% strain changes. **b**, GF-strain profiles of two suggested G_1 -1D sensors. Sensor 1: a G_1 -1D sensor with a MXene/SWNT/PVA ratio of 53/45/2 and sensing layer thickness of 924 nm. Sensor 2: a G_1 -1D sensor with a MXene/SWNT/PVA ratio of 40/60/0 and sensing layer thickness of 653 nm. **c**, Resistance-strain profile of Sensor 1 for monitoring a robotic task of grasping a candle. **d**, Resistance-strain profile of Sensor 1 for monitoring a robotic task of grasping a glue. **e**, Configuration of a soft swimmer robot with five model-suggested G_0 sensors. **f**, Simulated strain distribution map of symmetric pectoral fins achieved by finite element analysis. **g**, GF-strain profiles of two suggested G_0 sensors. Sensor 1: a G_0 sensor with MXene/SWNT/PVA ratio of 95/5/0 and sensing layer thickness of 1,484 nm. Sensor 2: a G_0 sensor with MXene/SWNT/PVA ratio of 95/5/0 and sensing layer thickness of 1,534 nm. **h**, Resistance-strain profile of an embedded G_0 sensor (Sensor 2) in the left fin of a soft swimmer robot.

no surface cracks were observed until 60% strain, initiating the formation of short and zigzagged cracks along the valley of isotropic crumples (see Supplementary Fig. 7a–c for in situ SEM images; further discussion can be found in in Supplementary Note 18.

Automatic strain sensor design for soft machines. The ultimate prediction model was employed to suggest feasible fabrication recipes of adequate strain sensors to monitor a soft pneumatic gripper (Supplementary Fig. 13)⁵³. From our rough estimation in Fig. 6a, the strain changes of a soft gripper during its reversible grasping behaviours ranged from 19% to 28%. By entering the design requests (that is, $GF > 100$ between 19% and 28%), several feasible fabrication recipes are suggested in Supplementary Table 7 (see Supplementary Note 19 for details), and the GF -strain profiles of two G_1 -1D sensors are shown in Fig. 6b. Both G_1 -1D sensors exhibited high sensitivity with $GF > 100$ within the designated strain range of 19–28%, which were able to collect the sensing signals in real time during the robotic grasping tasks (Fig. 6c,d). The stability of model-suggested sensors were tested and summarized in Supplementary Note 20.

The machine learning-enabled prediction model was next applied to realize automatic sensor design for the soft machines with complex actuations under extremely low strains $< 5\%$. Figure 6e and Supplementary Video 1 demonstrates a soft swimmer robot for underwater exploration that well mimicked the flapping behaviours of a batoids⁵⁴. Figure 6f presents a simulated strain distribution map on the symmetric pectoral fins of a swimmer robot, where the strain changes were extremely small at 0.8–1.0%. By inputting the design requests (that is, $GF > 100$ between 0.8% and 1.0%), several feasible fabrication recipes are suggested in Supplementary Table 8, and the GF -strain profiles of two G_0 sensors are characterized in Fig. 6g, exhibiting high sensitivity in terms of $GF > 100$ within the strain range of 0.8–1.0%. As demonstrated in Fig. 6h, Supplementary Fig. 14 and Supplementary Video 2, five suggested G_0 sensors (that is, Sensor 2) were then embedded within one pectoral fin, and their sensing signals were recorded in real time.

Conclusion

In this work, a hybrid approach through wet-lab experiments and machine intelligence was developed to construct a high-accuracy prediction model enabling automatic sensor design across a wide strain range (from $< 0.5\%$ to 350%), which was then applied to a variety of soft machines. We adopted three representative nanomaterials (MXene nanosheets, SWNTs and PVA binders) for the fabrication of strain-sensing layers for G_n sensors. A three-stage framework—including SVM classifier training, active learning loops and data augmentation—was realized to define the model's boundaries, enrich the multidimensional dataset and cultivate the model's prediction accuracy, respectively. To ensure data quality and balance, 351 delamination tests and 125 G_n sensors were conducted/fabricated by one lab under identical protocols with no literature data. After data augmentation and GA selection, the multidimensional dataset of ML-enabled prediction model contained $> 10,000$ real and virtual data points. Inverse design of strain sensors for diverse soft machines can be achieved automatically by using the ultimate prediction model without trial-and-error experiments. Further data analyses were executed to investigate several generalized design principles for G_n sensors as future references, which were further validated by in situ electron microscopic studies. The model-suggested G_n sensors were integrated into two kinds of soft machines, soft gripper and batoid-like swimmer, as the final demonstration.

Methods

Materials. Lithium fluoride (LiF, Sigma-Aldrich, BioUltra, $\geq 99.0\%$), hydrochloric acid (HCl, Sigma-Aldrich, ACS reagent, 37%), Ti_3AlC_2 MAX powders (MAX, Tongrun Info Technology), SWNTs (Timesnano), sodium dodecyl sulfate (SDS,

Sigma-Aldrich, $> 99.9\%$), PVA (Sigma-Aldrich, $M_n = 67,000$), ethanol (Thermo Fisher, $> 99.5\%$) and dichloromethane (DCM) (J.T. Baker, 99.9%) were used as received without further purification. Transparent polystyrene shrink films were purchased from Grafix. VHB Tape 4910 (2.54 cm \times 32.9 m) was purchased from 3M. Conductive silver paste was purchased from Ted Pella. Deionized water (18.2 M Ω) was obtained from a Milli-Q water purification system (Millipore) and used as the water source throughout this work.

Quantification of the degree of space exploration of the collected recipe labels. To represent the degree of space exploration, \bar{L} is calculated by equation (4):

$$\bar{L} = \frac{1}{N} \sum_{j=1}^N \left(\frac{1}{N} \sum_{i=1}^N \sqrt{\left(\begin{bmatrix} s_i \\ p_i \\ t_i \\ m_i \end{bmatrix} - \begin{bmatrix} s_j \\ p_j \\ t_j \\ m_j \end{bmatrix} \right)^2} \right), \quad (4)$$

where N is the cumulative number of data points; s, p, t , and m are the recipe labels (including SWNT loading, PVA loading, sensing layer thickness and morphology) of one data point, i ; and s, p, t , and m are the recipe labels of another data point, j .

Calculation of MSE. For the navigation model during active learning, the prediction accuracy of sensor performance is calculated by MSE defined in equation (5):

$$MSE = \frac{1}{N} \sum_{i=1}^N (\text{output}^i - E^i)^2, \quad (5)$$

where N is the cumulative number of test data (that is, $N = 30$); output^i is the model-predicted strain labels (ϵ_{10} , ϵ_{100} and ϵ_{\max}) on basis of the recipe labels of a test data point, i ; E^i is the actual strain values (ϵ_{10} , ϵ_{100} and ϵ_{\max}) of a test data point, i .

More detailed notes are provided in Supplementary Information.

Experimental section. Preparation of $Ti_3C_2T_x$ MXene nanosheets. $Ti_3C_2T_x$ MXene nanosheets were prepared according to the literature⁵⁵. LiF (1.0 g) was added to 6.0 M HCl solution (20 ml) under vigorous stirring. After the dissolution of LiF, 1.0 g of Ti_3AlC_2 MAX powder was slowly added into the HF-containing solution, and then the mixture was kept at 35 °C for 24 h. Afterwards, the solid residue was washed with deionized water several times until the pH value increased to around 7.0. The washed residue was subsequently added into 100 ml of deionized water, ultrasonicated for 1 h under N_2 atmosphere and centrifuged at 3,000 r.p.m. for 30 min. The supernatant was collected as the suspension of $Ti_3C_2T_x$ MXene nanosheets with an approximate concentration of 5 mg ml $^{-1}$.

Preparation of SWNT dispersion. The SWNT dispersion was obtained by adding SWNT powders into the SDS solution with a concentration of 2 mg ml $^{-1}$ (at a mass ratio of SWNT:SDS = 1:20). The mixture was then ultrasonicated by a probe sonicator for 2 h, and the concentration of final SWNT dispersion was about 0.1 mg ml $^{-1}$.

Preparation of PVA solution. 150 mg of PVA was dissolved in 30 ml of deionized water to obtain the PVA solution of 5 mg ml $^{-1}$, and the concentration of PVA solution was then adjusted to 0.05 mg ml $^{-1}$ for further use.

Deposition of ps-MXene layers. The mixtures of MXene/SWNT/PVA were prepared by mixing the MXene and SWNT dispersions and the PVA solution at various mass ratios, and the mixtures were then deposited on PVDF membranes (0.22 μ m pore, Merck Millipore) through a vacuum-assisted filtration system. After the deposition of MXene/SWNT/PVA mixtures on PVDF membranes, the planar ps-MXene layers were rinsed with excessive deionized water to remove SDS. The ps-MXene layers were further detached from PVDF membranes by immersing them in an ethanol bath, and the detached ps-MXene layers were stored in ethanol for the fabrication of G_n sensors afterwards. The composition of ps-MXene layer was managed to be controlled by tuning the volume ratio of MXene, SWNT and PVA dispersions/solution, and the thickness of ps-MXene layer was tuned by adjusting the areal mass loading during vacuum-assisted filtration.

Fabrication of G_0 sensors. A freestanding ps-MXene layer was carefully transferred onto a VHB tape in an ethanol bath followed by overnight drying. Copper wires were then connected to two ends of planar ps-MXene layer, and silver paste was applied at the connection joints to ensure good electrical contacts.

Fabrication of G_1 -1D sensors. Thermally responsive polystyrene substrate (also called shrink film) with uniaxial pre-strain was first cut into rectangles (with dimensions of 4 \times 8 cm 2), washed with ethanol and dried under nitrogen gas flow. The cut shrink films were next treated with oxygen plasma for 2 min to produce hydroxyl groups on the polystyrene surface, which enhanced the hydrophilic

interactions between polystyrene substrate and ps-MXene layer⁵⁶. Afterwards, the planar ps-MXene layer was carefully transferred onto the plasma-treated shrink film followed by overnight drying. The ps-MXene-coated polystyrene device was heated in an oven at 100 °C for 2.5 min to induce uniaxial shrinkage. The shrunk sample was then immersed in DCM to dissolve the polystyrene substrate to obtain a freestanding ps-MXene layer with wrinkle-like textures, which was sequentially rinsed with DCM, acetone and ethanol. The wrinkle-textured ps-MXene layers were stored in ethanol and carefully transferred onto a VHB tape followed by overnight drying for the fabrication of G_1 -1D sensors. Copper wires were connected to two ends of wrinkle-textured ps-MXene layer, and silver paste was applied at the connection joints to ensure good electrical contacts.

Fabrication of G_1 -2D sensors. Shrink film with biaxial pre-strain was first cut into rectangles (with the dimensions of 4 × 8 cm²), washed with ethanol, dried under nitrogen gas flow, and treated with oxygen plasma. The planar ps-MXene layer was then carefully transferred onto the plasma-treated shrink film followed by overnight drying. Afterward, the planar ps-MXene-coated polystyrene device was heated in an oven at 100 °C for 5 min without constraints for biaxial shrinkage. The shrunk sample was then immersed in DCM to dissolve the polystyrene substrate to obtain a freestanding ps-MXene layer with crumple-like textures, which was sequentially rinsed with DCM, acetone and ethanol. The crumple-textured ps-MXene layers were stored in ethanol and carefully transferred onto a VHB tape followed by overnight drying for the fabrication of G_1 -2D sensors. Copper wires were connected to two ends of crumple-textured ps-MXene layer, and silver paste was applied at the connection joints to ensure good electrical contacts.

Fabrication of a soft gripper and integration of model-suggested G_n sensors. A soft gripper was constructed by multiple bellows-type soft actuators, which were made of thermoplastic elastomers shaped from three-dimensionally printed moulds. Detailed fabrication steps of the soft gripper used in this work was described ref.⁵³. In brief, each bellows-type soft actuator consisted of one air channel, which was inflated on pressurization for bending. The robotic actuation of soft gripper was programmatically controlled by a microcontroller (Arduino) coupled with a pneumatic pump-valve system (Parker). Following positive gas pressure, the soft gripper was pneumatically inflated and bent along the long axis of its soft robotic body. Three soft actuators acted similar as human fingers to grasp objects, and higher positive gas pressure led to larger degrees of bending. As shown in Fig. 6a, the soft gripper was required to grasp two different objects (candle and superglue), and the uniaxial strain changes of grasping candle and superglue were quantified by using ImageJ to be 19% and 28%, respectively. According to the estimated strain changes, the ultimate prediction model suggested several feasible fabrication recipes for G_n sensors. Model-suggested G_n sensors were fabricated and attached onto the exterior surface of one soft actuator. During the robotic tasks, the resistance changes of model-suggested G_n sensor were monitored in real time using an electrochemical workstation (Metrohm Autolab Singapore Pte).

Fabrication of a soft swimmer robot and integration of model-suggested G_n sensors. A soft swimmer robot was composed from two major components: (1) the soft elastomeric body, including two large pectoral fins; and (2) the core shell housing all actuating components and electronics. Detailed fabrication of soft batoid-like swimmer robot can be found in ref.⁵⁴. Simulation of localized strain distribution map on the pectoral fins of soft swimmer robot was performed by FEA. The fin was modelled as a thin shell with uniform thickness yet varying bending rigidity, and the fin was assumed to be symmetric along the thickness direction. Eight-noded linear solid shell elements were used in the FEA simulations. According to the simulated strain changes, the ultimate prediction model suggested several feasible recipes for the fabrication of G_n sensors.

Model-suggested G_n sensors were integrated into the pectoral fins during the fabrication of soft swimmer robot by adhering two thin layers of silicon rubber (Ecoflex 0030). First, parts A and B of Ecoflex 0030 were mixed at a one-to-one mass ratio, and 0.2 wt% of yellow pigment was added. Five model-suggested G_n sensors were attached to the designated locations of one pectoral fin, and the silicon mixture was then poured into the three-dimensionally printed moulds for the encapsulation of G_n sensors, flapping bars and core shell (containing all actuating components and electronics). After a 24 h curing process, the soft swimmer robot was carefully removed from the moulds. During the flapping movements of soft swimmer robot, the resistance changes of five model-suggested G_n sensors were recorded in real time using an electrochemical workstation (Metrohm Autolab Singapore Pte).

FEA simulation. The three-dimensional models of ps-MXene structures with different surface morphologies were built by SolidWorks 2018, and the surface characteristics of ps-MXene were modelled by the Freeform feature. Afterwards, based on the established three-dimensional models, the FEA models of textured ps-MXene nanolayers were built by Static Structural module of ANSYS Workbench 19.0. The simulation parameters were set as follows: Young's modulus ~1.7 GPa, Poisson's ratio 0.227, and density 1.25 g cm⁻³. Cartesian was chosen for the mesh method, and the element size was set to be 100 µm. The FEA simulation was conducted as follows: the left boundary of the three-dimensional ps-MXene model

was fixed, while the right boundary was set to be movable. Uniaxial stretching was simulated by moving the right boundary, and the equivalent elastic strains and overall deformation were recorded.

Characterization. X-ray diffraction analysis was conducted using an X-ray diffractometer (Bruker, D8 Advance X-ray Powder Diffractometer, Cu K α (λ = 0.154 nm) radiation) at a scan rate of 4° min⁻¹. X-ray photoelectron spectra was recorded on an X-ray photoelectron spectrometer (Kratos AXIS Ultra^{DL}) via a microfocused Al X-ray beam (100 µm, 25 W), with a photoelectron take-off angle of 90°. Raman spectra were characterized by using HORIBA XploraPlus Microscope Raman. The morphology of as-exfoliated MXene nanosheets were characterized by using high-resolution transmission electron microscopy (JEOL 2010F). The surface morphologies and thicknesses of ps-MXene layers were characterized by using a SEM (FEI Quanta 600) and a field emission SEM (JEOL-JSM-6610LV) operating at 15.0 kV. The surface roughness of ps-MXene layers was measured by an AFM (Bruker Dimension ICON) with the operation mode of tapping in air. The resistance profiles of the G_0 , G_1 -1D and G_1 -2D sensors under various uniaxial strains were measured by Industrial Multimeter (REX503). A fatigue test was performed on a G_n sensor for 1,000 cycles under repeated uniaxial strains by a tensile tester (Instron 5543, Instron) with a 500-N load cell, and the resistance changes of the G_0 , G_1 -1D and G_1 -2D sensors were monitored in real time using an electrochemical workstation (Metrohm Autolab Singapore Pte).

Reporting Summary. Further information on research design is available in the Nature Research Reporting Summary linked to this article.

Data availability

The data that support the plots within this paper and other findings of this study are available from the corresponding authors on reasonable request. Source data are provided with this paper.

Code availability

The Python code to implement the machine learning tasks within this study are available from GitHub (https://github.com/jiali1025/Automatic_Strain_Sensor_Design) or Zenodo (<https://doi.org/10.5281/zenodo.5709148>)⁵⁷.

Received: 18 January 2021; Accepted: 7 December 2021;

Published online: 26 January 2022

References

- Rus, D. & Tolley, M. T. Design, fabrication and control of soft robots. *Nature* **521**, 467–475 (2015).
- Shepherd, R. F. et al. Multigait soft robot. *Proc. Natl Acad. Sci. USA* **108**, 20400–20403 (2011).
- Walsh, C. Human-in-the-loop development of soft wearable robots. *Nat. Rev. Mater.* **3**, 78–80 (2018).
- Rus, D. & Tolley, M. T. Design, fabrication and control of origami robots. *Nat. Rev. Mater.* **3**, 101–112 (2018).
- Kim, Y., Yuk, H., Zhao, R., Chester, S. A. & Zhao, X. Printing ferromagnetic domains for untethered fast-transforming soft materials. *Nature* **558**, 274–279 (2018).
- Hu, W., Lum, G. Z., Mastrangeli, M. & Sitti, M. Small-scale soft-bodied robot with multimodal locomotion. *Nature* **554**, 81–85 (2018).
- Laschi, C., Mazzolai, B. & Cianchetti, M. Soft robotics: technologies and systems pushing the boundaries of robot abilities. *Sci. Rob.* **1**, eaah3690 (2016).
- Kim, Y., Parada, G. A., Liu, S. & Zhao, X. Ferromagnetic soft continuum robots. *Sci. Rob.* **4**, eaax7329 (2019).
- Wang, M. et al. Gesture recognition using a bioinspired learning architecture that integrates visual data with somatosensory data from stretchable sensors. *Nat. Electron.* **3**, 563–570 (2020).
- Zhou, Z. et al. Sign-to-speech translation using machine-learning-assisted stretchable sensor arrays. *Nat. Electron.* **3**, 571–578 (2020).
- Thuruthel, T. G., Shih, B., Laschi, C. & Tolley, M. T. Soft robot perception using embedded soft sensors and recurrent neural networks. *Sci. Robot.* **4**, eaav1488 (2019).
- Sinatra, N. R. et al. Ultrgentle manipulation of delicate structures using a soft robotic gripper. *Sci. Robot.* **4**, eaax5425 (2019).
- Sundaram, S. et al. Learning the signatures of the human grasp using a scalable tactile glove. *Nature* **569**, 698–702 (2019).
- Zhang, J. et al. Robotic artificial muscles: current progress and future perspectives. *IEEE Trans. Robot.* **35**, 761–781 (2019).
- Mirvakili, S. M. & Hunter, I. W. Artificial muscles: mechanisms, applications, and challenges. *Adv. Mater.* **30**, 1704407 (2018).
- Zhao, H., O'Brien, K., Li, S. & Shepherd, R. F. Optoelectronically innervated soft prosthetic hand via stretchable optical waveguides. *Sci. Robot.* **1**, eaai7529 (2016).

17. Cianchetti, M., Laschi, C., Menciassi, A. & Dario, P. Biomedical applications of soft robotics. *Nat. Rev. Mater.* **3**, 143–153 (2018).
18. Amjadi, M., Kyung, K.-U., Park, I. & Sitti, M. Stretchable, skin-mountable, and wearable strain sensors and their potential applications: A review. *Adv. Funct. Mater.* **26**, 1678–1698 (2016).
19. Qiu, A. et al. A path beyond metal and silicon: polymer/nanomaterial composites for stretchable strain sensors. *Adv. Funct. Mater.* **29**, 1806306 (2019).
20. Cai, Y. et al. Stretchable $\text{Ti}_3\text{C}_2\text{T}_x$ MXene/carbon nanotube composite based strain sensor with ultrahigh sensitivity and tunable sensing range. *ACS Nano* **12**, 56–62 (2018).
21. Shi, X., Liu, S., Sun, Y., Liang, J. & Chen, Y. Lowering internal friction of 0D–1D–2D ternary nanocomposite-based strain sensor by fullerene to boost the sensing performance. *Adv. Funct. Mater.* **28**, 1800850 (2018).
22. Wang, Y. et al. Wearable and highly sensitive graphene strain sensors for human motion monitoring. *Adv. Funct. Mater.* **24**, 4666–4670 (2014).
23. Shi, X. et al. Bioinspired ultrasensitive and stretchable MXene-based strain sensor via nacre-mimetic microscale 'brick-and-mortar' architecture. *ACS Nano* **13**, 649–659 (2019).
24. Jayathilaka, W. A. D. M. et al. Significance of nanomaterials in wearables: A review on wearable actuators and sensors. *Adv. Mater.* **31**, 1805921 (2019).
25. Araromi, O. A. et al. Ultra-sensitive and resilient compliant strain gauges for soft machines. *Nature* **587**, 219–224 (2020).
26. Yang, H. et al. Wireless $\text{Ti}_3\text{C}_2\text{T}_x$ MXene strain sensor with ultrahigh sensitivity and designated working windows for soft exoskeletons. *ACS Nano* **14**, 11860–11875 (2020).
27. Wang, H., Totaro, M. & Beccai, L. Toward perceptive soft robots: progress and challenges. *Adv. Sci.* **5**, 1800541 (2018).
28. Mengüç, Y. et al. Wearable soft sensing suit for human gait measurement. *Int. J. Rob. Res.* **33**, 1748–1764 (2014).
29. Lu, N. & Kim, D.-H. Flexible and stretchable electronics paving the way for soft robotics. *Soft Robot.* **1**, 53–62 (2014).
30. Schmidt, J., Marques, M. R. G., Botti, S. & Marques, M. A. L. Recent advances and applications of machine learning in solid-state materials science. *npj Comput. Mater.* **5**, 83 (2019).
31. Xia, B. et al. Improving the actuation speed and multi-cyclic actuation characteristics of silicone/ethanol soft actuators. *Actuators* **9**, 62 (2020).
32. Butler, K. T., Davies, D. W., Cartwright, H., Isayev, O. & Walsh, A. Machine learning for molecular and materials science. *Nature* **559**, 547–555 (2018).
33. Zahrt, A. F. et al. Prediction of higher-selectivity catalysts by computer-driven workflow and machine learning. *Science* **363**, eaau5631 (2019).
34. Toyao, T. et al. Machine learning for catalysis informatics: recent applications and prospects. *ACS Catal.* **10**, 2260–2297 (2020).
35. Kitchin, J. R. Machine learning in catalysis. *Nat. Catal.* **1**, 230–232 (2018).
36. Vamathevan, J. et al. Applications of machine learning in drug discovery and development. *Nat. Rev. Drug Discov.* **18**, 463–477 (2019).
37. Ekins, S. et al. Exploiting machine learning for end-to-end drug discovery and development. *Nat. Mater.* **18**, 435–441 (2019).
38. Voznyy, O. et al. Machine learning accelerates discovery of optimal colloidal quantum dot synthesis. *ACS Nano* **13**, 11122–11128 (2019).
39. Durrer, R. et al. Automated tuning of double quantum dots into specific charge states using neural networks. *Phys. Rev. Appl.* **13**, 054019 (2020).
40. Li, J. et al. AI applications through the whole life cycle of material discovery. *Matter* **3**, 393–432 (2020).
41. Cole, J. M. A design-to-device pipeline for data-driven materials discovery. *Acc. Chem. Res.* **53**, 599–610 (2020).
42. Cao, B. et al. How to optimize materials and devices via design of experiments and machine learning: demonstration using organic photovoltaics. *ACS Nano* **12**, 7434–7444 (2018).
43. Afsarimanesh, N. et al. A review on fabrication, characterization and implementation of wearable strain sensors. *Sens. Actuator A* **315**, 112355 (2020).
44. Murphey, Y. L., Guo, H. & Feldkamp, L. A. Neural learning from unbalanced data. *Appl. Intell.* **21**, 117–128 (2004).
45. Hoffmann, J. et al. Machine learning in a data-limited regime: augmenting experiments with synthetic data uncovers order in crumpled sheets. *Sci. Adv.* **5**, eaau6792 (2019).
46. Chen, P.-Y. et al. Multiscale graphene topographies programmed by sequential mechanical deformation. *Adv. Mater.* **28**, 3564–3571 (2016).
47. Noble, W. S. What is a support vector machine? *Nat. Biotechnol.* **24**, 1565–1567 (2006).
48. Whitley, D. A genetic algorithm tutorial. *Stat. Comput.* **4**, 65–85 (1994).
49. Schober, P., Boer, C. & Schwarte, L. A. Correlation coefficients: appropriate use and interpretation. *Anesth. Analg.* **126**, 1763–1768 (2018).
50. Štrumbelj, E. & Kononenko, I. Explaining prediction models and individual predictions with feature contributions. *Knowl. Inf. Syst.* **41**, 647–665 (2014).
51. Bach, S. et al. On pixel-wise explanations for non-linear classifier decisions by layer-wise relevance propagation. *PLoS ONE* **10**, e0130140 (2015).
52. Zhang, S. et al. Predicting the formability of hybrid organic-inorganic perovskites via an interpretable machine learning strategy. *J. Phys. Chem. Lett.* **12**, 7423–7430 (2021).
53. Low, J. H. et al. Hybrid tele-manipulation system using a sensorized 3-D-printed soft robotic gripper and a soft fabric-based haptic glove. *IEEE Robot. Autom. Lett.* **2**, 880–887 (2017).
54. Truong, T. V., Viswanathan, V. K., Joseph, V. S. & Alvarado, P. V. Y. Design and characterization of a fully autonomous under-actuated soft batoid-like robot. In *2019 IEEE/RSJ International Conference on Intelligent Robots and Systems (IROS)* 5826–5831 (IEEE, 2019).
55. Alhabeb, M. et al. Guidelines for synthesis and processing of two-dimensional titanium carbide ($\text{Ti}_3\text{C}_2\text{T}_x$ MXene). *Chem. Mater.* **29**, 7633–7644 (2017).
56. Shenton, M. J., Lovell-Hoare, M. C. & Stevens, G. C. Adhesion enhancement of polymer surfaces by atmospheric plasma treatment. *J. Phys. D* **34**, 2754–2760 (2001).
57. Li, J., Lim, K. & Yang, H. Automatic strain sensor design (v.1.0.3). *Zenodo* <https://doi.org/10.5281/zenodo.5709148> (2021).

Acknowledgements

We thank C.-H. Yeow from the Department of Biomedical Engineering in the National University of Singapore for providing the soft gripper. We acknowledge the financial support provided by the Singapore RIE2020 Advanced Manufacturing and Engineering Programmatic Grant 'Accelerated Materials Development for Manufacturing' by the Agency for Science, Technology and Research under grant no. A1898b0043 (to X.W.). We acknowledge the financial support provided by the Start-Up Fund of University of Maryland, College Park (KFS no. 2957431 to P.-Y.C.). Funding for this research was provided by Maryland Industrial Partnerships under grant no. 6808 (KFS no. 4311103 to P.-Y.C.), Maryland Innovation Initiative (MII) Technology Assessment Award (KFS no. 4308302 to P.-Y.C.), and MOST-AFOSR Taiwan Topological and Nanostructured Materials Grant under grant no. FA2386-21-1-4065 (KFS no. 5284212 to P.-Y.C.).

Author contributions

P.-Y.C., X.W., J.L. and H.Y. conceived the project ideas and designed the experiments. H.Y. and S.L. carried out the synthesis of MXene nanosheets and characterizations. H.Y., K.Z.L. and J.L. designed the machine learning framework and implemented the machine learning tasks in Python. H.Y., Q.W., J.L. and C.P. collected the experimental data. T.V.T., Q.W. and H.Y. integrated the model-suggested sensors onto soft swimmer robot and performed related tests. X.X. and H.Y. performed the FEA simulations and analyses. P.-Y.C., X.W., J.L. and H.Y. interpreted the results and co-wrote the manuscript. K.L., S.L., M.D., T.C., X.L. and Q.X. involved in the discussion and manuscript revisions. P.-Y.C., P.V.A. and X.W. supervised this project.

Competing interests

The authors declare no competing interests.

Additional information

Extended data is available for this paper at <https://doi.org/10.1038/s42256-021-00434-8>.

Supplementary information The online version contains supplementary material available at <https://doi.org/10.1038/s42256-021-00434-8>.

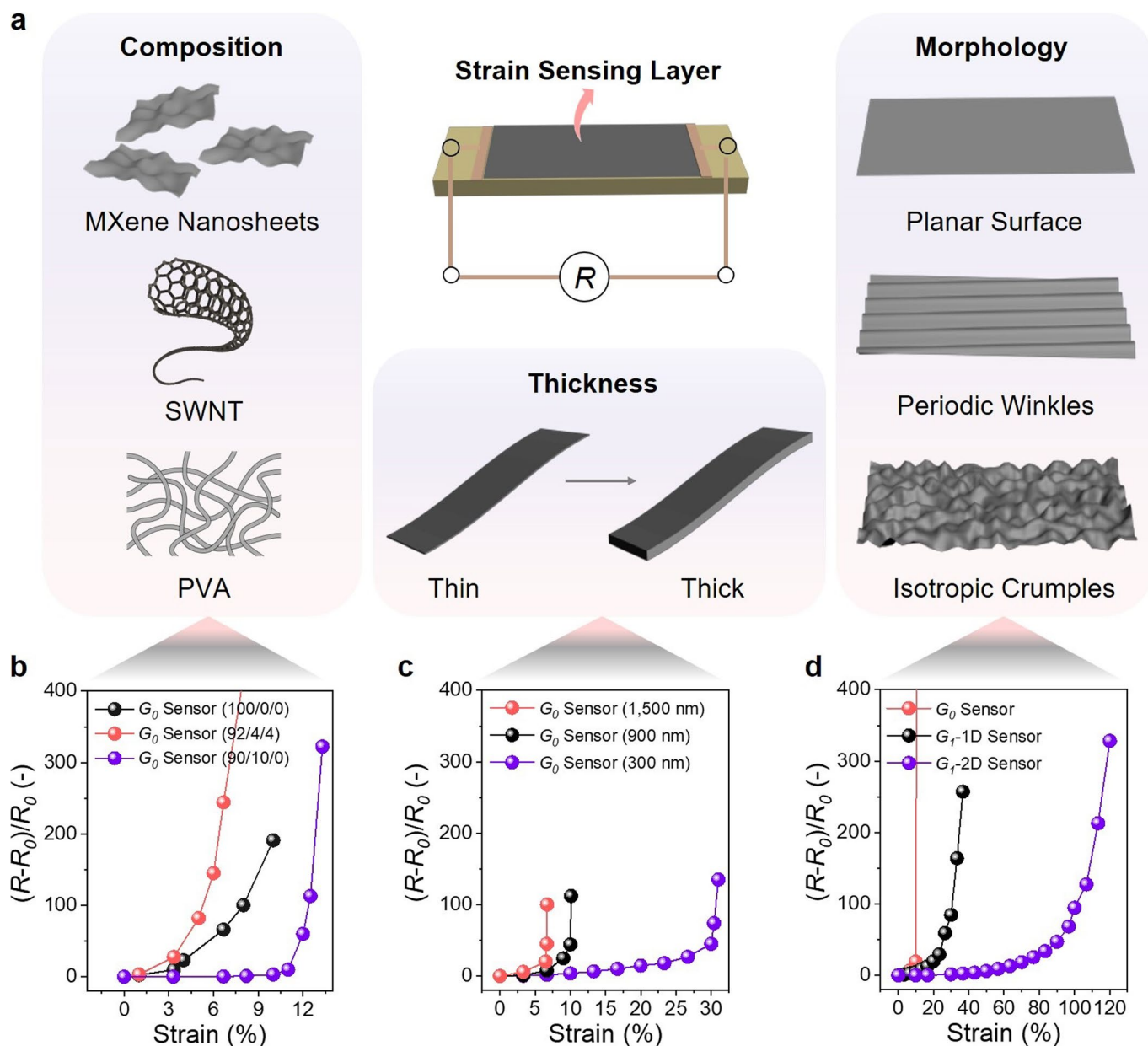
Correspondence and requests for materials should be addressed to Xiaonan Wang or Po-Yen Chen.

Peer review information *Nature Machine Intelligence* thanks the anonymous reviewers for their contribution to the peer review of this work.

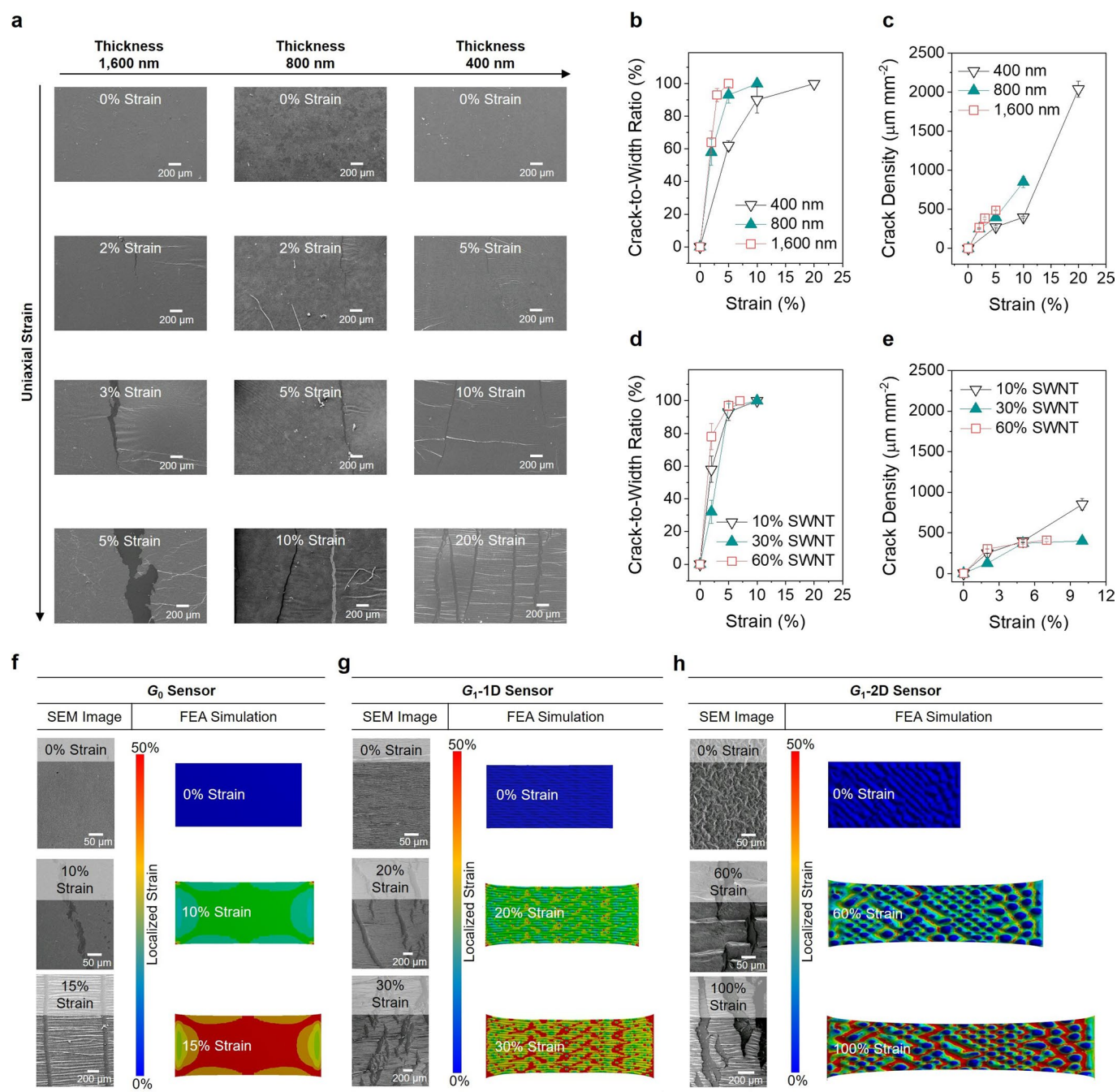
Reprints and permissions information is available at www.nature.com/reprints.

Publisher's note Springer Nature remains neutral with regard to jurisdictional claims in published maps and institutional affiliations.

© The Author(s), under exclusive licence to Springer Nature Limited 2022, corrected publication 2022



Extended Data Fig. 1 | Influential fabrication parameters for tuning strain sensor characteristics. (a) Schematic illustration of influential fabrication parameters for tuning strain sensor characteristics, including composition, thickness, and morphology of strain sensing layer. (b) Resistance-strain profiles of various G_0 sensors with the sensing layers at different MXene/SWNT/PVA ratios. All G_0 sensors were with the sensing layers at the same thickness of 800 nm. (c) Resistance-strain profiles of various G_0 sensors with the sensing layers at different thicknesses. All G_0 sensors were with the sensing layers at the same MXene/SWNT/PVA ratio of 90/5/5. (d) Resistance-strain profiles of G_n sensors with different sensing layer morphologies. All G_n sensors were composed of ps-MXene layers either with planar texture (G_0), periodic wrinkles (G_r -1D) or isotropic crumples (G_r -2D). The MXene/SWNT/PVA ratio and thickness of all ps-MXene layers were controlled to be 100/0/0 and 800 nm, respectively.



Extended Data Fig. 2 | *In situ* electron microscopic studies to validate data-driven design rules. (a) SEM images of G_0 ps-MXene layers with varying thicknesses under various uniaxial strains. Crack-to-width ratios (b) and crack densities (c) in G_0 ps-MXene layers with varying thicknesses. All the ps-MXene layers kept the same MXene/SWNT/PVA ratio of 90/10/0. Crack-to-width ratios (d) and crack densities (e) in G_0 ps-MXene layers with varying SWNT loadings (wt.%). All the ps-MXene layers kept the same thickness of 800 nm and 0 wt.% PVA loading. FEA simulation of strain distribution and *in situ* SEM images of G_0 (f), G_1 -1D (g), and G_1 -2D (h) ps-MXene layers under various uniaxial strains.

Reporting Summary

Nature Portfolio wishes to improve the reproducibility of the work that we publish. This form provides structure for consistency and transparency in reporting. For further information on Nature Portfolio policies, see our [Editorial Policies](#) and the [Editorial Policy Checklist](#).

Statistics

For all statistical analyses, confirm that the following items are present in the figure legend, table legend, main text, or Methods section.

- | | |
|-------------------------------------|--|
| n/a | Confirmed |
| <input type="checkbox"/> | <input checked="" type="checkbox"/> The exact sample size (n) for each experimental group/condition, given as a discrete number and unit of measurement |
| <input type="checkbox"/> | <input checked="" type="checkbox"/> A statement on whether measurements were taken from distinct samples or whether the same sample was measured repeatedly |
| <input type="checkbox"/> | <input checked="" type="checkbox"/> The statistical test(s) used AND whether they are one- or two-sided
<i>Only common tests should be described solely by name; describe more complex techniques in the Methods section.</i> |
| <input checked="" type="checkbox"/> | <input type="checkbox"/> A description of all covariates tested |
| <input type="checkbox"/> | <input checked="" type="checkbox"/> A description of any assumptions or corrections, such as tests of normality and adjustment for multiple comparisons |
| <input type="checkbox"/> | <input checked="" type="checkbox"/> A full description of the statistical parameters including central tendency (e.g. means) or other basic estimates (e.g. regression coefficient) AND variation (e.g. standard deviation) or associated estimates of uncertainty (e.g. confidence intervals) |
| <input type="checkbox"/> | <input checked="" type="checkbox"/> For null hypothesis testing, the test statistic (e.g. F , t , r) with confidence intervals, effect sizes, degrees of freedom and P value noted
<i>Give P values as exact values whenever suitable.</i> |
| <input checked="" type="checkbox"/> | <input type="checkbox"/> For Bayesian analysis, information on the choice of priors and Markov chain Monte Carlo settings |
| <input checked="" type="checkbox"/> | <input type="checkbox"/> For hierarchical and complex designs, identification of the appropriate level for tests and full reporting of outcomes |
| <input type="checkbox"/> | <input checked="" type="checkbox"/> Estimates of effect sizes (e.g. Cohen's d , Pearson's r), indicating how they were calculated |

Our web collection on [statistics for biologists](#) contains articles on many of the points above.

Software and code

Policy information about [availability of computer code](#)

Data collection

Data analysis

For manuscripts utilizing custom algorithms or software that are central to the research but not yet described in published literature, software must be made available to editors and reviewers. We strongly encourage code deposition in a community repository (e.g. GitHub). See the Nature Portfolio [guidelines for submitting code & software](#) for further information.

Data

Policy information about [availability of data](#)

All manuscripts must include a [data availability statement](#). This statement should provide the following information, where applicable:

- Accession codes, unique identifiers, or web links for publicly available datasets
- A description of any restrictions on data availability
- For clinical datasets or third party data, please ensure that the statement adheres to our [policy](#)

All the figures and raw data are provided in the main manuscript and Supplementary Information. The Python codes to implement active learning and automatic sensor design in this study are available at GitHub with the link: https://github.com/jiali1025/Automatic_Strain_Sensor_Design.

Field-specific reporting

Please select the one below that is the best fit for your research. If you are not sure, read the appropriate sections before making your selection.

☐ Life sciences ☐ Behavioural & social sciences ☐ Ecological, evolutionary & environmental sciences

For a reference copy of the document with all sections, see [nature.com/documents/nr-reporting-summary-flat.pdf](https://www.nature.com/documents/nr-reporting-summary-flat.pdf)

Life sciences study design

All studies must disclose on these points even when the disclosure is negative.

Sample size	n/a
Data exclusions	n/a
Replication	n/a
Randomization	n/a
Blinding	n/a

Behavioural & social sciences study design

All studies must disclose on these points even when the disclosure is negative.

Study description	n/a
Research sample	n/a
Sampling strategy	n/a
Data collection	n/a
Timing	n/a
Data exclusions	n/a
Non-participation	n/a
Randomization	n/a

Ecological, evolutionary & environmental sciences study design

All studies must disclose on these points even when the disclosure is negative.

Study description	n/a
Research sample	n/a
Sampling strategy	n/a
Data collection	n/a
Timing and spatial scale	n/a
Data exclusions	n/a
Reproducibility	n/a
Randomization	n/a
Blinding	n/a

Did the study involve field work? ☐ Yes ☒ No

Reporting for specific materials, systems and methods

We require information from authors about some types of materials, experimental systems and methods used in many studies. Here, indicate whether each material, system or method listed is relevant to your study. If you are not sure if a list item applies to your research, read the appropriate section before selecting a response.

Materials & experimental systems

n/a	Involved in the study
<input checked="" type="checkbox"/>	<input type="checkbox"/> Antibodies
<input checked="" type="checkbox"/>	<input type="checkbox"/> Eukaryotic cell lines
<input checked="" type="checkbox"/>	<input type="checkbox"/> Palaeontology and archaeology
<input checked="" type="checkbox"/>	<input type="checkbox"/> Animals and other organisms
<input checked="" type="checkbox"/>	<input type="checkbox"/> Human research participants
<input checked="" type="checkbox"/>	<input type="checkbox"/> Clinical data
<input checked="" type="checkbox"/>	<input type="checkbox"/> Dual use research of concern

Methods

n/a	Involved in the study
<input checked="" type="checkbox"/>	<input type="checkbox"/> ChIP-seq
<input checked="" type="checkbox"/>	<input type="checkbox"/> Flow cytometry
<input checked="" type="checkbox"/>	<input type="checkbox"/> MRI-based neuroimaging